Hindawi

Research Article

Nonharmonic Control of the Blade-Vortex Interaction Noise of Electrically Controlled Rotor

Kewei Li [1,2,3] **Taoyong Su** [1,3] **Yang Lu** [2] **and Qijun Zhao** [2]

¹*School of General Aviation, Nanchang Hangkong University, Nanchang 330063, China*
²*National Key Laboratory of Rotorcraft Aeromechanics, College of Aerospace Engineering, Nanjing University of Aeronautics and Astronautics, Nanjing 210016, China*
³*Rotor Aerodynamics Key Laboratory, China Aerodynamics Research and Development Center, Mianyang Sichuan 621000, China*

Correspondence should be addressed to Taoyong Su; sutaoyong@126.com

Electrically controlled rotor, also known as swashplateless rotor, represents an active rotor system that, due to the use of a trailing edge flap system instead of a swashplate, not only enables primary control but also conveniently reduces the blade-vortex interaction (BVI) noise of the rotors through active control. The effect of nonharmonic inputs on the control of the BVI noise of electrically controlled rotors based on their unique trailing edge flap systems has been investigated in this paper. To this end, an analytical model for the vortex interaction-induced load and noise of electrically controlled rotor is first established based on the viscous vortex particle method, the Weissinger-L blade model, and the Ffowcs Williams-Hawkings (FW-H) equation. On this basis, a simulation study of flap nonharmonic control for BVI noise reduction in electrically controlled rotors is carried out. According to the mechanism of the BVI in electrically controlled rotors, the second quadrant flap nonharmonic control is used to reduce the advancing side BVI noise, and the effects of different control waveforms and amplitudes on the peak value and directivity of the BVI noise of the sample electrically controlled rotors are analyzed to reveal the noise reduction mechanism of flap nonharmonic control. Subsequently, the effect of the third quadrant flap nonharmonic control on BVI noise on the retreating side of the sample electrically controlled rotors is investigated. The results show that flap nonharmonic control has little effect on miss distance and that it controls BVI noise mainly by reducing the wake vortex strength on the advancing and retreating sides, which may lead to an increase in rotor noise in other regions; the noise reduction effect of flap nonharmonic control for different blade preindex angles indicates that suitable preindex angles coupled with flap nonharmonic control help optimally reduce noise.

1. Introduction

Electrically controlled rotor (ECR), also known as swashplateless rotors, employ a trailing edge flap system for primary control [1]. As the swashplate is eliminated, the control system of the electrically controlled rotors can be simplified, which can effectively reduce the empty weight and the parasite drag of the helicopter. At present, researches on electrically controlled rotors are mainly focused on feasibility analysis [2], aeroelastic dynamics modeling [3, 4], design parameter analysis [5], and performance enhancement [6].

However, rotors represent not only the primary lifting and control surface of a helicopter but also the most signifi-

cant source of the helicopter's external field noise. Rotor noise is usually divided into rotation noise, BVI noise, high-speed impulse (HSI) noise, and broadband noise [7]; the mechanism of rotor noise generation varies depending on its type, and there are also differences in noise intensity and propagation direction. BVI noise is essentially a pulsing load noise; when a helicopter is in oblique descent and maneuvering flight, the blade tip vortex released by the trailing edge of the rotor blade interacts with the following blade, resulting in impulsive changes in blade airloads and radiating BVI noise. When BVI noise appears, it significantly enhances the level of the midfrequency noise (200 Hz–2000 Hz) of the helicopter, and the human ear is very

sensitive to this frequency component [8]. Moreover, BVI noise principally propagates out of the rotor rotation plane, which may result in serious noise pollution in the spaces in front of and below the helicopter. Therefore, reducing the BVI noise of rotors has been a popular research topic in the field of helicopters.

At present, helicopter rotor BVI noise control techniques mainly include the maneuverability method, passive method, and active method. The maneuverability method does not directly change the characteristics of the rotor blade tip vortex but rather alters the entire aerodynamic environment to avoid the occurrence of a BVI state or to reduce the BVI intensity when it does occur, for example, by limiting the helicopter's flight trajectory [9], adjusting its flight attitude [10], and changing the rotor speed [11]. The passive method focuses on changing the aerodynamic configuration of rotor blades to reduce the intensity of the blade tip vortex and to increase the distance of BVI; researchers are currently concentrating on new blade tip shapes, such as the Ogee tip [12], the inverted dihedral tip [13], and the British Experimental Rotor Programme (BERP) tip [14], all of which have demonstrated favorable BVI noise reduction capabilities; in addition, the research findings in reference [15] indicate that the leading edge serrated blade is also effective in reducing rotor BVI noise resulting from blade-vortex parallel interaction. Due to the restrictions of aerodynamic and dynamic design requirements for rotor blades, the passive method has limited effects on reducing BVI noise, so in recent years, increasing numbers of scholars have begun to study active control techniques for reducing rotor BVI noise. Of the various active control methods for reducing rotor BVI noise, the actively controlled flap (ACF) technique has been proven to be effective in reducing BVI noise in numerical simulations and wind tunnel tests [16–23]; thus, it is considered one of the most promising active control methods for rotors [24]. Essentially, the trailing edge flap system of electrically controlled rotors is an active control device that can be used to reduce BVI noise from electrically controlled rotors if appropriate active control is adopted.

Our previous research on the generation mechanism of electrically controlled rotor BVI has demonstrated that there are not only concentrated blade tip vortices in the wake flow field of electrically controlled rotors but there are also strong flap tip vortices when the flap deflection is significant [4]; the flap tip vortices released in the second quadrant convect downstream and produce the advancing side interactions, while the blade tip vortices released in the third quadrant convect downstream and produce the retreating side interactions [25]. At present, research on active control methods based on ACFs is focused on single-frequency harmonic and combined harmonic control; based on the BVI generation mechanism of electrically controlled rotors, nonharmonic inputs are introduced in the local azimuth range to reduce the wake vortex strength at the corresponding azimuth position, which can not only reduce the BVI-induced noise of electrically controlled rotors but also reduce the dependence on the closed-loop control system to some extent. As rotor BVI loads and BVI-induced noise depend mainly on wake

vortex strength, BVI distance, and angle, accurate prediction of the spatial position of the wake and the effect of flap deflection is fundamental to the study of electrically controlled rotor BVI noise control; therefore, we propose to first model the aerodynamics of an electrically controlled rotor using the viscous vortex particle method, which can effectively capture the distorted motion of the electrically controlled rotor wake vorticity [26–31]; on this basis, nonharmonic inputs of the flap are applied in the second and third quadrants to reduce the wake vortex strength at the corresponding azimuths, enabling nonharmonic control of the BVI noise of the electrically controlled rotor.

This paper consists of the following sections. Section 2 describes a model for calculating electrically controlled rotor BVI airloads and noise developed by the viscous vortex particle method, the Weissinger-L lifting surface method, and the Farassat 1A BVI noise radiation integral formula and presents the electrically controlled rotor trim equation for coupled flap nonharmonic control. Section 3 presents the generation mechanism of the BVI of an electrically controlled rotor and the effect of the blade preindex angle, on the basis of which the effect of different types of flap nonharmonic inputs on the control of electrically controlled rotor BVI noise is investigated. Finally, the conclusion of this paper is outlined in Section 4.

2. Nonharmonic Control Model for BVI Noise of ECR

This section principally covers the viscous vortex particle wake model, the Weissinger-L lifting surface model, the BVI-induced noise computing model, and the flap nonharmonic control scheme.

2.1. Viscous Vortex Particle Wake Model. The high Reynolds number rotor wake vortex field can be represented by the noncompressible Navier-Stokes equation in the vorticity-velocity form under the Lagrange system; the viscous vortex particle method uses vortex particles with certain vorticity to disperse the continuous vortex field, and the discretized equation of vortex dynamics can be expressed as the convection-diffusion form of N vortex particles:

$$\frac{D\boldsymbol{x}_i}{Dt} = \boldsymbol{u}(\boldsymbol{x}_i, t), \tag{1}$$

$$\frac{D\boldsymbol{\alpha}_i}{Dt} = \boldsymbol{\alpha}_i \cdot \nabla \boldsymbol{u}(\boldsymbol{x}_i, t) + \nu \nabla^2 \boldsymbol{\alpha}_i + S, \tag{2}$$

where $\boldsymbol{\alpha}_i$ and $\boldsymbol{x}_i$ are the vorticity vector and position vector of vortex particle, respectively, at time point t; $\boldsymbol{u}$ represents the local velocity vector; ν denotes the kinematic viscosity; D/Dt is the material derivative, and S is the local vorticity source.

The first term on the right of Equation (2) is a stretch term, which represents the effect of stretching and bending on the local vorticity; the second term is a viscosity diffusion

term, which reflects the vortex diffusion effect caused by the fluid viscosity; the third term is a source term indicating that new vortexes are constantly being generated on the rotor blades and escaping into the rotor wake. The velocity gradient in the stretch term includes the induced velocity gradient caused by the vortex particles in the rotor wake and the rotor blades, where the induced velocity gradient resulting from vortex particles is determined by the direct method:

$$\boldsymbol{\alpha}_i \cdot \nabla \boldsymbol{u}_{ip}(\boldsymbol{x}_i, t) = \left[\sum_{j=1}^{N} \frac{1}{\sigma_{ij}^3} \left[\tilde{\boldsymbol{\alpha}}_j \right] \left[\nabla \left(K(\rho) \left(\boldsymbol{x}_i - \boldsymbol{x}_j \right) \right) \right] \right] \cdot \boldsymbol{\alpha}_i, \quad (3)$$

where $[\tilde{\boldsymbol{\alpha}}_j]$ is the antisymmetric tensor induced by the vorticity vector of the vortex particles, σ denotes the smooth radius of a vortex particle, and $K(\rho)$ represents the smooth-corrected Biot-Savart kernel function.

The viscosity diffusion terms are determined by the particle intensity exchange method [26]:

$$\nu \nabla^2 \boldsymbol{\alpha}_i = \frac{2\nu}{\sigma_{ij}^2} \sum_{j=1}^{N} \left(V_i \boldsymbol{\alpha}_j - V_j \boldsymbol{\alpha}_i \right) \xi_{\sigma_{ij}} \left(\boldsymbol{x}_i - \boldsymbol{x}_j \right), \quad (4)$$

where V is the volume of a vortex particle and $\xi_\sigma(\boldsymbol{x} - \boldsymbol{x}_i)$ represents the smooth-corrected vortex particle vorticity distribution function.

In this paper, the Adams-Bashforth time integration algorithm with 2nd-order accuracy is used to determine the location and vortex strength of the vortex particles, and the wake convergence is reached after the revolution of the rotor exceeds a certain prescribe threshold. Reference [4] contains a detailed description of the viscous vortex wake method for ECR.

2.2. Weissinger-L Lifting Surface Model of an ECR Blade.
The source term in Equation (2) needs to be determined by means of a blade model. In this paper, the Weissinger-L lifting surface model is employed to determine the spanwise variation in the ECR blade bound vortex circulation along the span direction and the location of the shedding point and vortex strength of the new vortex particles.

Figure 1 illustrates a schematic diagram of the determination of the vortex lattice attached to an electrically controlled rotor blade and the new vortex elements. The spanwise variation in the vorticity attached to blade and the variation with the azimuth result in the trailing vorticity in the direction of rotation and the shed vorticity in the blade span direction, respectively.

A control point is arranged at the blade 3/4 chord in each vortex lattice, and the relationship between the vorticity attached to the blade and the local induced velocity is established, taking into account the impenetrability of the object plane. Due to the introduction of trailing edge flaps, the electrically controlled rotor blade employs an equivalent geometric angle of attack at the flap segment, and the effect of flap deflection and overhang balance on

the normal vector of local object plane is determined as follows:

$$\alpha_{\text{eff}} = \alpha + \frac{1}{\pi} \left(T_{10} - l T_{21} \right) \delta, \quad (5)$$

where α_{eff} is the equivalent incidence of the flap segment airfoil for the ECR blade, α is the geometric incidence of the flap segment basic airfoil, δ is the flap deflection angle, and downward deflection is positive, l is the nondimensional flap overhang corresponding to the semichord length of the airfoil, and T_{10} and T_{21} are constants related to the flap chordwise location. For detailed expressions, please refer to reference [32].

Since the offset of the near wake induced by the flap deflection is much less than the flow field resolution, the analysis model did not take into account its effect. For the same reason, the effect of the flap deflection on the control point is also not considered.

Following the identification of the distribution of the vortexes attached to the blades, the near wake vortex lattice is replaced by an equivalent vortex particle; then, the source term in Equation (2) can be expressed as

$$S = -\frac{d\boldsymbol{\omega}_b}{dt} + \boldsymbol{u}_b \nabla \cdot \boldsymbol{\omega}_b, \quad (6)$$

where $\boldsymbol{\omega}_b$ is the bound vorticity of the blade segment and $\boldsymbol{u}_b$ denotes the velocity vector of the blade segment relative to the air.

Once the iterations of rotor wake and bound circulation converge, the unsteady airloads of the airfoil and the incremental airloads caused by trailing edge flap motion are obtained by using Leishman-Beddoes model [33] and Hariharan-Leishman model [34], respectively.

2.3. Computational Model of Aerodynamic Noise in the BVI Condition.
The calculation of rotor aerodynamic noise is based on the Ffowcs Williams-Hawkings (FW-H) equation [35]. Since BVI usually occurs during the oblique descent of the rotor, the quadrupole noise component contributes little to the overall noise field; the noise is calculated in this paper through the Farassat 1A formula obtained by neglecting the quadrupole noise source term in the FW-H equation. $p'(\boldsymbol{x}, t)$ denotes the total sound pressure at an observation point, and we have the following:

$$p'(\boldsymbol{x}, t) = p'_T(\boldsymbol{x}, t) + p'_L(\boldsymbol{x}, t), \quad (7)$$

where

$$
\begin{aligned}
p'_T(\boldsymbol{x}, t) = & \frac{1}{4\pi} \int_{f=0} \left[\frac{\rho_0 \dot{V}_n}{r(1 - M_{ar})^2} \right]_{\text{ret}} ds \\
& + \frac{1}{4\pi} \int_{f=0} \left[\frac{\rho_0 V_n \left(r \dot{M}_{ai} \hat{r}_i + c_0 M_{ar} - c_0 M_a^2 \right)}{r^2 (1 - M_{ar})^3} \right]_{\text{ret}} ds,
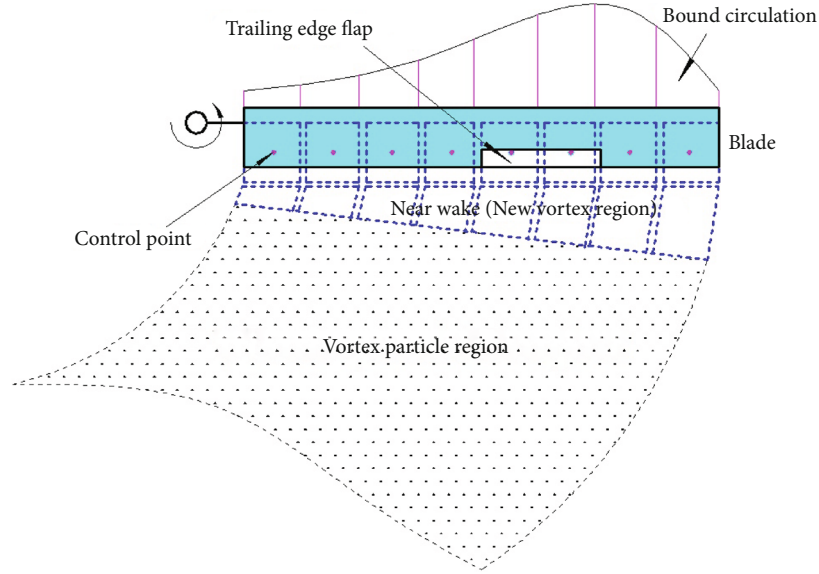\end{aligned}
$$

$$(8)$$

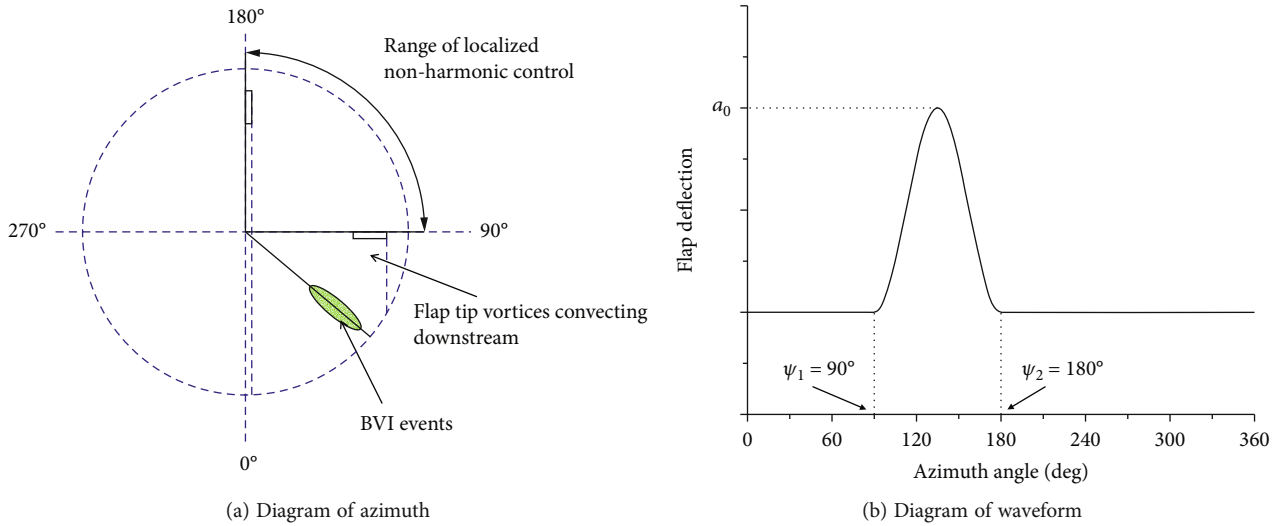FIGURE 1: Solution diagram of the vortex lattice bound to the ECR blade surface and new vortex particle.

(a) Diagram of azimuth

(b) Diagram of waveform

FIGURE 2: Schematic diagram of the azimuth and waveform of the cosine input in the second quadrant of flap.

$$
p'_L(\boldsymbol{x}, t) = \frac{1}{4\pi c_0} \left(\int_{f=0} \left[\frac{\dot{l}_i \widehat{r}_i}{r(1 - M_{ar})^2} \right]_{\text{ret}} ds \right.
$$
$$
+ \int_{f=0} \left[\frac{l_r \left(r \dot{M}_{ai} \widehat{r}_i + c_0 M_{ar} - c_0 M_a^2 \right)}{r^2 (1 - M_{ar})^3} \right]_{\text{ret}} ds \right) \quad (9)
$$
$$
+ \frac{1}{4\pi} \int_{f=0} \left[\frac{l_r - l_i M_{ai}}{r^2 (1 - M_{ar})^2} \right]_{\text{ret}} ds,
$$

where $p'_T(\boldsymbol{x}, t)$ represents the thickness noise, $p'_L(\boldsymbol{x}, t)$ is the load noise, superscript "$\cdot$" indicates the derivation of a parameter with respect to the delay time, M_{ai} denotes the component of the Mach number of the motion of the object plane in direction x_i, M_a is the motion Mach number of the

object plane, $\widehat{r}_i$ stands for the component of the unit vector radius in the direction of noise radiation to the observation point in the x_i direction, l_r is the projection of the force of the load on the object plane element on the local fluid in the direction of noise radiation, and c_0 is the sound speed in quiescent medium.

2.4. Flap Nonharmonic Control Scheme. ECR primary control is implemented via flap deflection, and the control variable is the flap deflection angle. In this paper, the control quantity of the electrically controlled rotor is the flap collective pitch δ_0, the longitudinal cycle variable pitch δ_{1s}, the flap lateral cyclic pitch δ_{1c}, and the nonharmonic control quantity δ_A; during the trimming, the effect of nonharmonic inputs on the trimming result of flap control is considered,
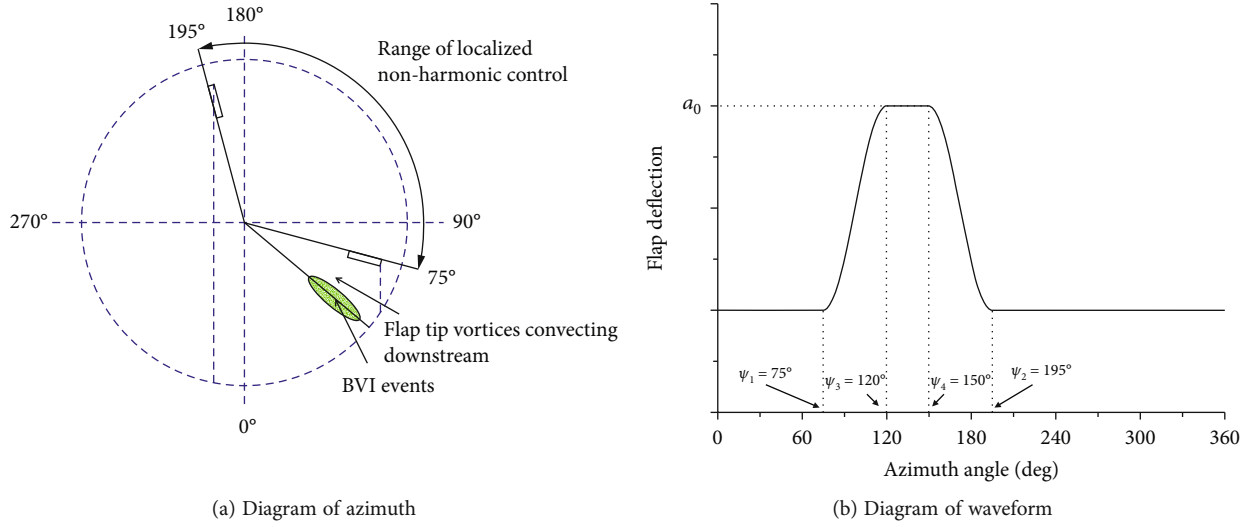
(a) Diagram of azimuth

(b) Diagram of waveform

FIGURE 3: Schematic diagram of the azimuth and waveform of the oblique square wave input in the second quadrant of flap.

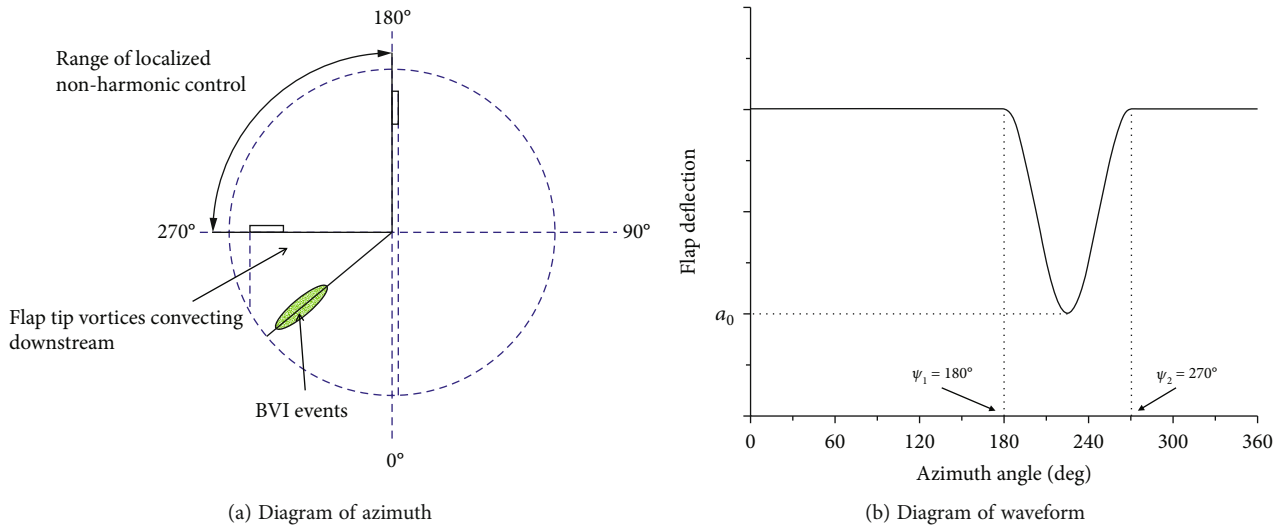

(a) Diagram of azimuth

(b) Diagram of waveform

FIGURE 4: Schematic diagram of the azimuth and waveform of the cosine input in the third quadrant of the flap.

so the flap deflection angle δ varies with azimuth ψ, as shown in Equation (10), where the downward deflection of the flap is positive.

$$\delta = \delta_0 + \delta_c \cos \psi + \delta_s \sin \psi + \delta_A. \qquad (10)$$

The findings of our previous study regarding the mechanism of the BVI of an electrically controlled rotor indicate that the BVI phenomenon on the advancing side of rotor principally occurs because the flap has a larger downward deflection angle in the second quadrant and the strong flap tip vortexes move with the incoming flow to the first quadrant and interact with the blade; the BVI phenomenon on the retreating side is similar to that of a conventional rotor and is principally caused by the interaction of the blade tip vortex from the third quadrant with the blade in the fourth

quadrant [25]. Therefore, for the advancing side BVI noise control, the nonharmonic amplitude of the flap should be negative to reduce the downward deflection of the electrically controlled rotor flap on the advancing side, which in turn reduces the flap tip vortex and ultimately reduces the BVI-induced noise on the advancing side of the electrically controlled rotor; for the retreating side BVI noise control, the nonharmonic amplitude of flap should be positive to reduce the pitch of electrically controlled rotor blade on the retreating side through the air-elastic action, which in turn reduces the blade tip vortex and ultimately reduces the BVI-induced noise on the retreating side of the electrically controlled rotor.

Specifically, we first investigate the effect of nonharmonic inputs in the cosine form in the second quadrant on BVI noise on the advancing side of the electrically controlled rotor (Scheme A).

(a) Diagram of azimuth
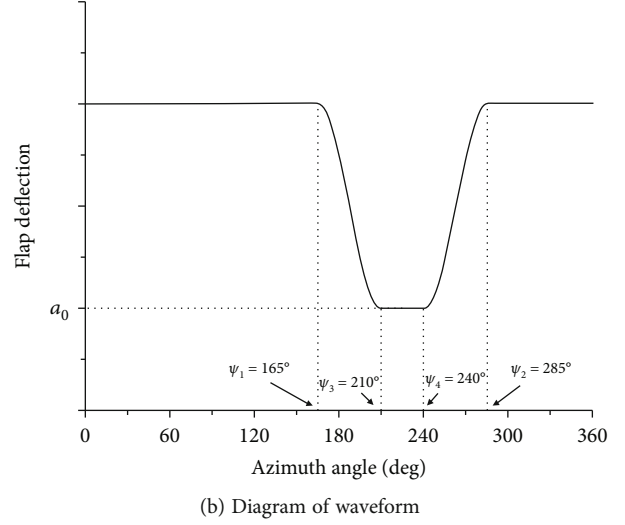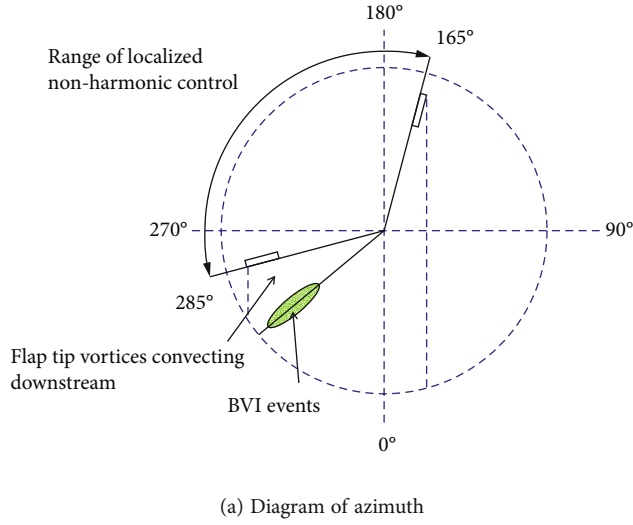

(b) Diagram of waveform

FIGURE 5: Schematic diagram of the azimuth and waveform of the oblique square wave input in the third quadrant of the flap.

TABLE 1: Key parameters of the sample electrically controlled rotor.

Parameter (unit)	Value
Torsional stiffness of the rotor root (Nm/rad)	95
Chord length of the flap (m)	0.03025
Span of the flap (m)	0.4
Spanwise center of the flap (m)	1.4
Dimensionless overhang balance of the flap	0.125

The functional expression of Scheme A is as follows:

$$\delta_A(\psi, \psi_1, \psi_2) = \frac{a_0}{2}\left[1 - \cos\left(\frac{2\pi(\psi - \psi_1)}{\psi_2 - \psi_1}\right)\right], \quad (11)$$

where a_0 is the amplitude of the nonharmonic input to the flap, $\psi_1 = 90°$ represents the starting azimuth applied for control, and $\psi_2 = 180°$ denotes the ending azimuth applied for control. The azimuth and waveform of the nonharmonic input are shown in Figure 2; for control of BVI noise on the advancing side of the electrically controlled rotor, the flap nonharmonic input amplitude a_0 is negative to reduce the downward deflection angle of the trailing edge flap on the advancing side of the electrically controlled rotor, thereby reducing the intensity of the flap tip vortex generated in the second quadrant.

According to the waveform of the cosine function, Scheme A yields the maximum value of the nonharmonic input only at a particular azimuth in the second quadrant; if the input maximum can be maintained in the second quadrant over a range of azimuth, the BVI intensity can be reduced over a wider span of the blade surface to achieve better noise reduction; therefore, we further investigate the effect of nonharmonic input in the form of oblique square wave in the second quadrant on the control of BVI noise on the advancing side of electrically controlled rotor (Scheme B).
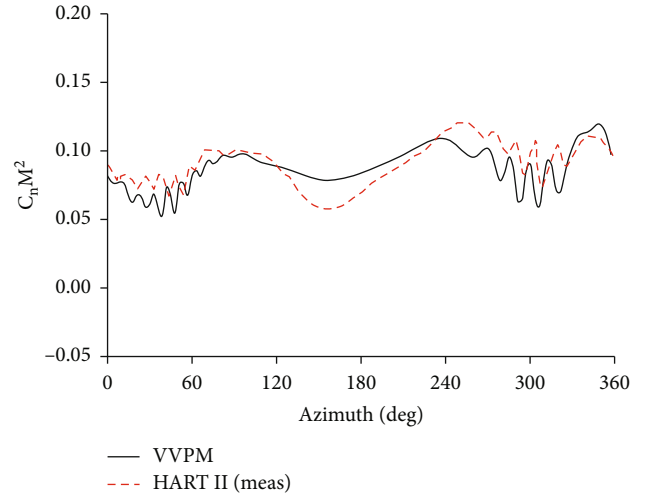

FIGURE 6: Normal force (C_nM^2) predictions at 87% radial station.

To ensure the continuity of the control waveform derivative and the slopes on both sides of the waveform are the same as those in Scheme A, the oblique square wave input used in Scheme B is still a cosine function on both sides, while the flap deflection angle is set to maintain a range of 30°, so its input azimuth range is 75°-195°; the expression is as follows:

$$\delta_A(\psi, \psi_1, \psi_2) = \begin{cases} \frac{a_0}{2}\left[1 - \cos\left(\frac{2\pi(\psi - \psi_1)}{2(\psi_3 - \psi_1)}\right)\right], & \psi_1 \leq \psi < \psi_3, \\ a_0 & \psi_3 \leq \psi \leq \psi_4, \\ \frac{a_0}{2}\left[1 - \cos\left(\frac{2\pi(\psi + \psi_2 - 2\psi_4)}{2(\psi_2 - \psi_4)}\right)\right], & \psi_4 < \psi \leq \psi_2, \end{cases}$$

$$(12)$$

where a_0 is the amplitude of the local nonharmonic input, $\psi_1 = 75°$ represents the starting azimuth applied for
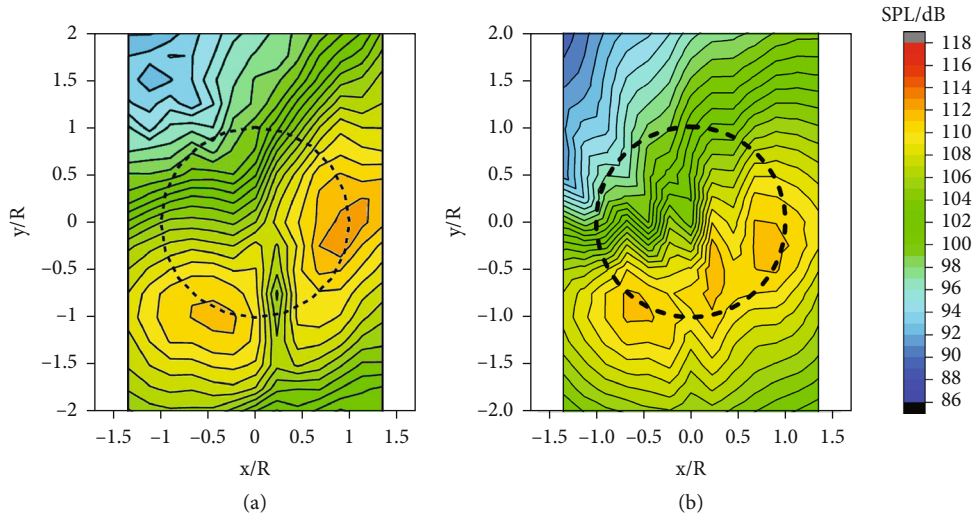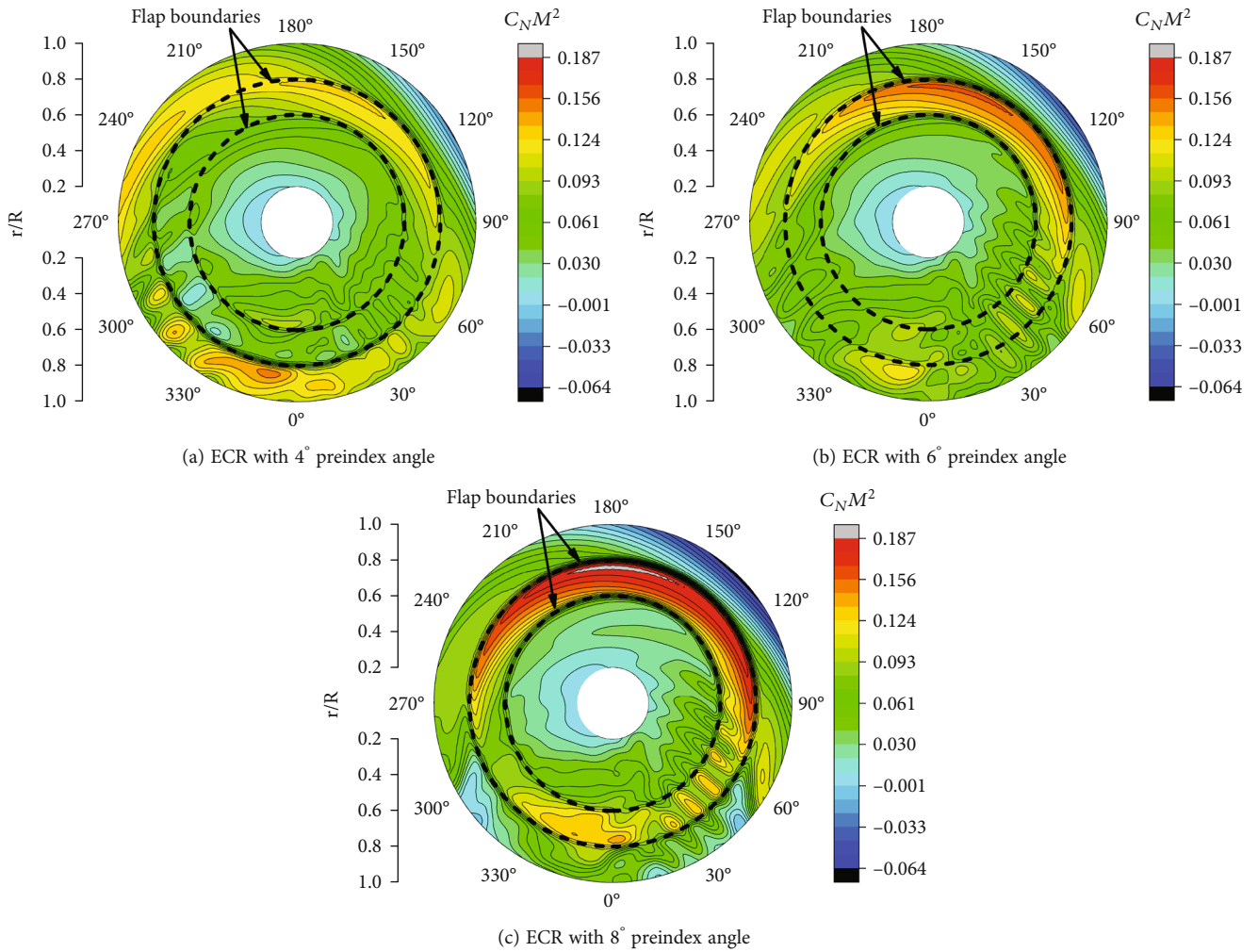
Figure 7: Predicted and measured SPL noise contours.

(a) ECR with 4° preindex angle

(b) ECR with 6° preindex angle

(c) ECR with 8° preindex angle

Figure 8: Disc airload distribution of the ECR.

(a) ECR with 4° preindex angle

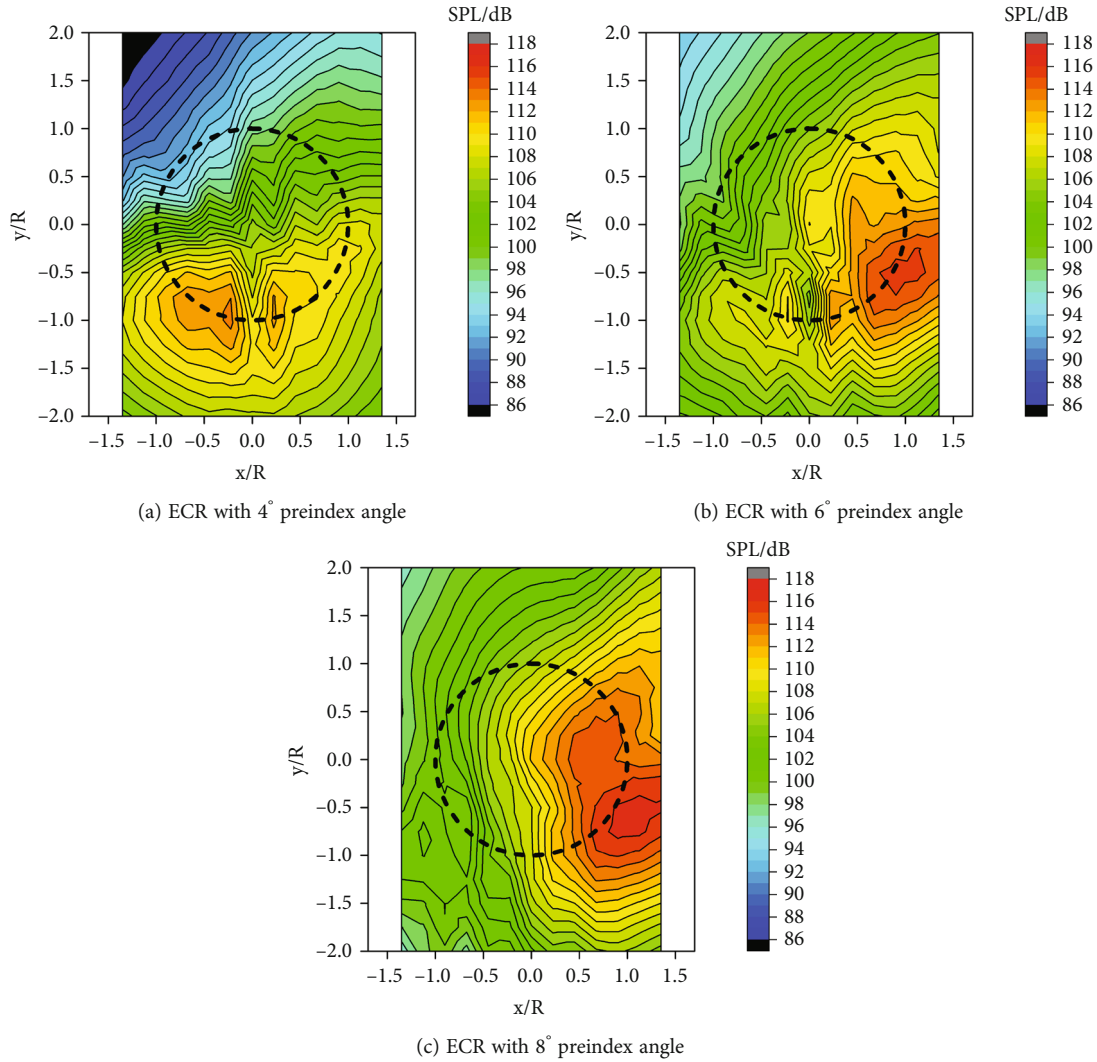(b) ECR with 6° preindex angle

(c) ECR with 8° preindex angle

FIGURE 9: Sound pressure level noise contours (6th-40th blade passage frequency).

control, and $\psi_2 = 195°$ denotes the ending azimuth applied for control. $\psi_3 = 120°$. The segment ending at $\psi_4 = 150°$ is the flap deflection angle holding segment; the azimuth applied for control and the waveform for Scheme B is shown in Figure 3.

For the BVI noise on the retreating side of electrically controlled rotor, the same two forms of nonharmonic input as described above are used; that is, in Scheme C, the cosine input is in the third quadrant; in Scheme D, the oblique square wave input is in the third quadrant. The expression of the nonharmonic input to the flap of Scheme C is the same as Equation (11); the range of the azimuth applied for the control is 180°-270°, but the input has a positive amplitude, i.e., an increase in the downward deflection angle of the flap; the input azimuth and waveform for Scheme C are shown in Figure 4.

The expression of the nonharmonic input to the flap of Scheme D is the same as Equation (12); the range of azimuth applied for the control is 165°-285°, but the input has a pos-

itive amplitude; the input azimuth and waveform for Scheme D are shown in Figure 5.

3. Results and Analysis

3.1. Sample ECR BVI Load and Noise. The accuracy of a model developed based on the viscous vortex method to predict the ECR BVI load and noise and analyzed the effect of blade preindex angle parameters, which is defined as the blade pitch at three-quarter span station when the ECR is stationary, specific to ECR blades on such load and noise is presented in reference [25]. To ensure the integrity of the paper, the calculated results of the sample ECR parameters and the ECR BVI load and noise at various preindex angles are given in this paper; the detailed model validation and analysis of the results are presented in reference [25].

In this paper, the test rotor of higher harmonic control aeroacoustic rotor test (HART) II [36] is taken as a benchmark and convert it into a sample ECR. The HART II test
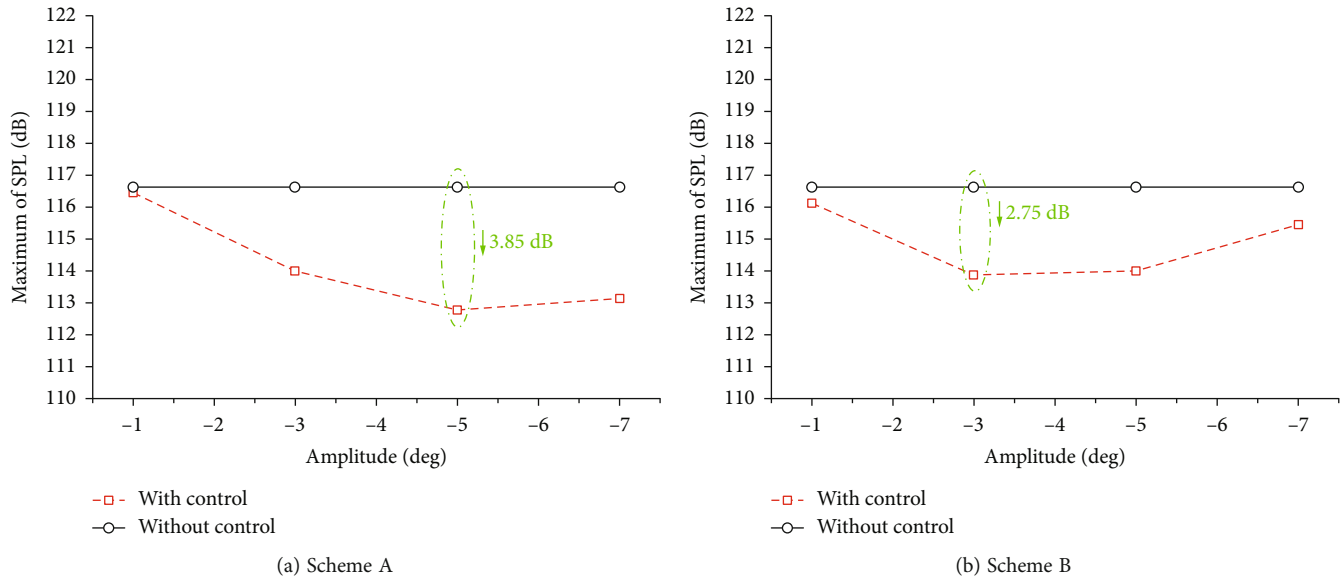
(a) Scheme A

(b) Scheme B

FIGURE 10: Effect of flap local nonharmonic inputs on maximum sound pressure level of the noise from ECR.

rotor has four hingeless blades with a rectangular tip, and the radius, chord, linear twist, and precone of the rotor are 2 m, 0.121 m, -8°, and 2.5°, respectively. The rotor was operated at an advance ratio of 0.151, with a rotor shaft angle of attack of 5.3°. The wind tunnel interference angle is -0.8°, which means that the effective angle of attack is reduced from 5.3° to approximately 4.5°. During the test, the rotor had a thrust coefficient of 0.00457. The main parameters of the sample ECR are shown in Table 1; the remaining parameters of it are the same as those of the HART II test rotor.

Currently, there are few ECR-related tests, and there is no literature regarding BVI-induced airloads and noise of ECR. Therefore, in this section, the HART II test BL case is used as an example to validate the present BVI-induced airloads and noise predicted model by comparing the blade airloads and the noise footprint on a horizontal plane below the rotor hub. In order to capture the BVI events, the results for the cases in this paper were obtained with an azimuthal step of 3°. Figure 6 shows the comparison of the predicted and experimental section normal force $C_n M^2$ at 87% span location. The predicted airloads fluctuate dramatically around 50° azimuth angle on the advancing side and around 300° on the retreating side, which is compared well with the experimental data. However, since the elastic deformation of the blade is not considered in the present analytical model, there are some discrepancies between the predicted airloads and the experimental data. Figure 7 shows the comparison between the predicted and measured BVI noise footprint on a horizontal plane below the rotor hub. The meaning of the circle drawn with dashed line is the projection of the rotor tip path. The simulation results show that two distinct radiation lobes appear in the advancing and retreating sides, which is the same with the experimental data obtained from the HART II test. The location and magnitude of the SPL maximum on the retreating side are an agreement with the measurements very well, while the magnitude of the SPL

maximum on the advancing side is slightly underestimated by 2-3 dB. In addition, the predicted BVI noise in the center and to the rear of the rotor disc is larger than the measured data because the effect of the fuselage on the absorption and scattering of noise is not considered in the simulation. The compared results show that the present model is capable of predicting the rotor BVI-induced airloads and noise.

Reference [25] analyzed the BVI load and noise characteristics for the sample ECR with preindex angles of 4°, 6°, and 8°, as shown in Figures 8 and 9. The BVI noise footprints of ECR are predicted on a horizontal plane placed 1.1075R below the rotor hub. The results of the study show that there are significant differences in the BVI loads and noise of ECR for various blade preindex angles; the most serious BVI is observed on the retreating side of the sample electrically controlled rotor when the blade preindex angle is 4°, while the most serious interaction is observed on the advancing side when the blade preindex angle is 8°. Therefore, we investigate the effect of flap nonharmonic inputs on the control of BVI noise on the retreating side and advancing side of the sample ECR with preindex angles of 4° and 8°, respectively.

3.2. Nonharmonic Control of the Advancing Side BVI Load and Noise of the Sample ECR.
To analyze the effect of the flap nonharmonic input on the control of the BVI noise on the advancing side of ECR, the maximum values of sound pressure level (SPL) in the rectangular region (8m × 5.4m) below the rotor blade at 6-40 times the blade passage frequency are presented in Figure 10 for input amplitudes a_0 -1°, -3°, -5°, and -7° of Schemes A and B.

Figure 10 shows that the maximum value of the sound pressure level under the rotor tends to decrease and then increase with increasing input amplitude for both nonharmonic input schemes. In this case, for the second quadrant cosine input used in Scheme A, the maximum values of

(a) Distribution of sound pressure levels when $a_0 = -3°$

(b) Difference in sound pressure level when $a_0 = -3°$

(c) Distribution of sound pressure levels when $a_0 = -5°$

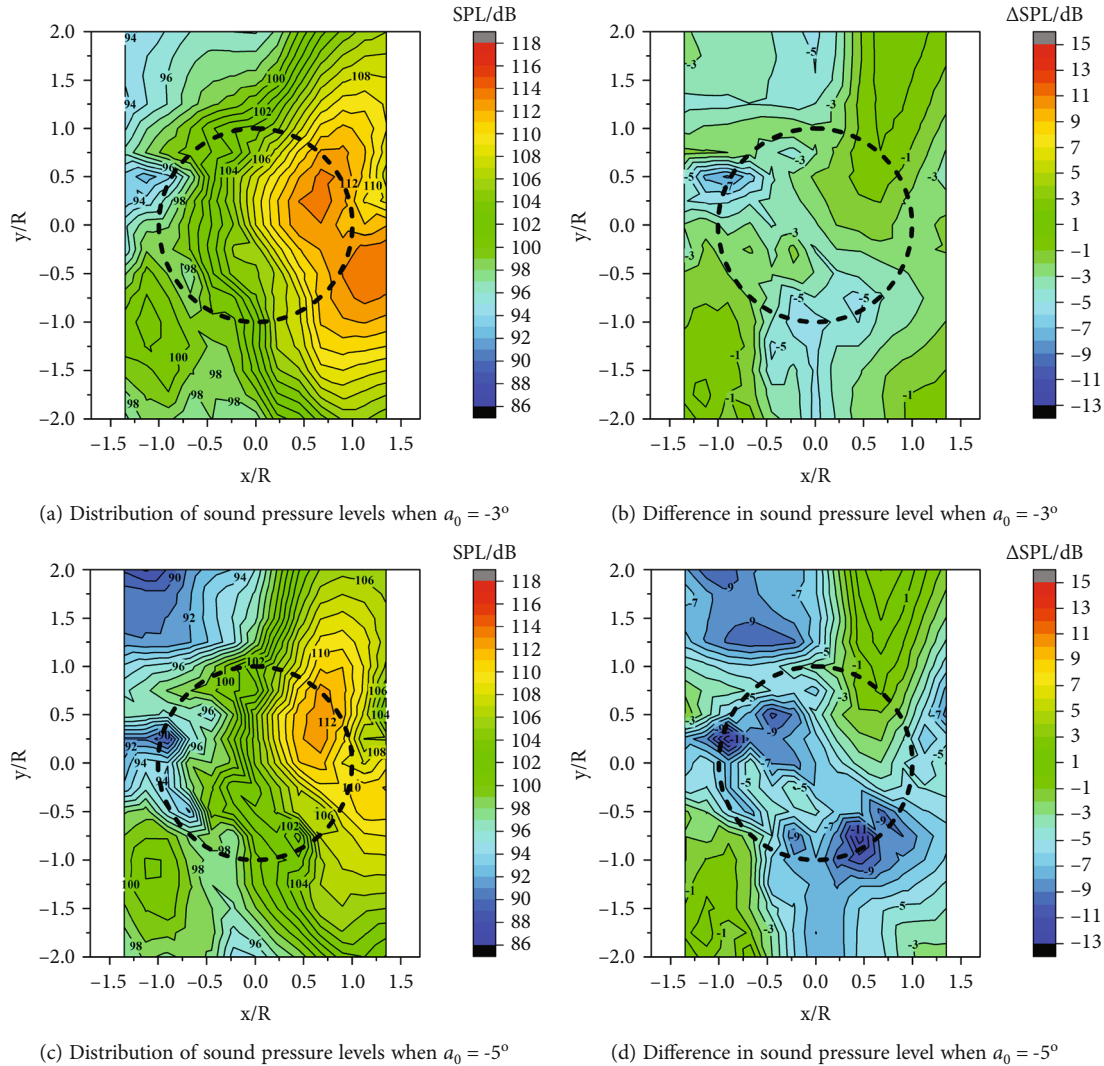(d) Difference in sound pressure level when $a_0 = -5°$

FIGURE 11: Distribution of SPL below the ECR under Scheme A and their difference from the SPL in the reference state.

the sound pressure level at different input amplitudes are smaller than that in the reference state; furthermore, the best control of noise under the ECR is achieved at an input amplitude of -5°, with the maximum value of the sound pressure level being reduced by approximately 3.85 dB compared with that of the reference state. For the second quadrant oblique square wave input used in Scheme B, the maximum values of the sound pressure level at different input amplitudes are lower than that in the reference state; furthermore, the best control of noise under the ECR is achieved at an input amplitude of -3°, with the maximum value of the sound pressure level being reduced by approximately 2.75 dB compared with that of the reference state. The second quadrant cosine input used in Scheme A offers a better control effect than in Scheme B in terms of the reduction in the maximum sound pressure level.

Figures 11 and 12 further show the distribution of sound pressure levels in the rectangular region (8m × 5.4m) below the sample ECR at 6-40 times the blade passage frequency for various nonharmonic control schemes with flap amplitudes a_0 of -3° and -5°, as well as the difference in sound

pressure levels from that of the reference state (ECR at a preindex angle of 8°). As can be seen from the figures, the BVI noise behind the advancing side of the ECR ($x/R > 0, y/R < 0$) is reduced when nonharmonic control is applied, but there is a varying increase in the sound pressure level in front of the ECR ($y/R > 0$).

For the second quadrant cosine input under Scheme A, there is some reduction in the sound pressure level below the ECR when the input amplitude is -3°; when the input amplitude is -5°, a significant reduction in sound pressure level is observed in all regions except for a 2 dB increase in the sound pressure level in front of the advancing side ($x/R > 0, y/R > 0$) of the ECR; the maximum reduction in the sound pressure level of BVI noise is approximately 11 dB behind the advancing side ($x/R > 0, y/R < 0$) and approximately 11 dB on the retreating side, with a maximum reduction of approximately 9 dB in front of the retreating side ($x/R < 0, y/R > 0$).

For the second quadrant oblique square wave input used in Scheme B, the control of noise under the ECR is less effective than that in in Scheme A when the input amplitude is
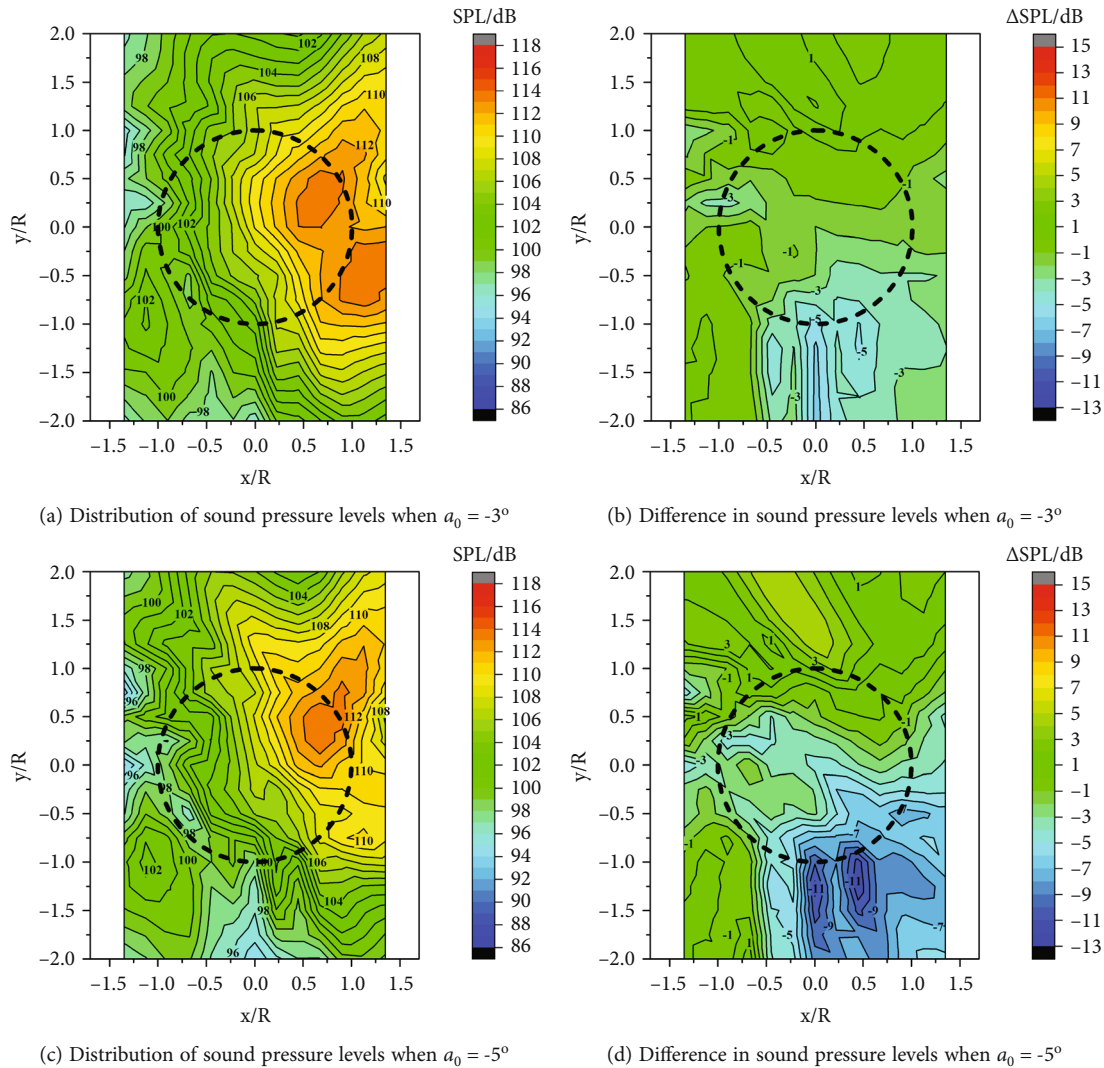
(a) Distribution of sound pressure levels when $a_0 = -3°$

(b) Difference in sound pressure levels when $a_0 = -3°$

(c) Distribution of sound pressure levels when $a_0 = -5°$

(d) Difference in sound pressure levels when $a_0 = -5°$

FIGURE 12: Distribution of SPL below the ECR under Scheme B and their difference from the SPL in the reference state.

-3°; when the input amplitude is -5°, the region of BVI noise reduction behind the advancing side of the ECR ($x/R > 0, y/R < 0$) is greater in extent than that in Scheme A, and the magnitude of noise reduction is comparable; however, there is no significant noise reduction in the other regions under the rotor. Thus, Scheme B is not as effective as Scheme A in terms of overall noise control under the rotor blades.

To analyze the noise reduction mechanism of the local nonharmonic input to the flap, the effect of the nonharmonic input to the flap on the load distribution of the sample ECR disc at an input amplitude of -5° is compared, as shown in Figure 13. As can be seen from the figure, the BVI load in the first quadrant on the advancing side of the sample ECR is reduced with both flap nonharmonic inputs, while the retreating side rotor disc load distribution is not significantly different from when nonharmonic control is not applied. This indicates that the reduction in noise behind the advancing side of the sample ECR is principally due to the nonharmonic input reducing the BVI load intensity in the first quadrant.

As mentioned above, the advancing side BVI of the ECR is mainly caused by the flap tip vortex; Figure 14 shows a comparison of the effect of the flap nonharmonic input on the tip vorticity of the sample ECR; from this, we can analyze the mechanism by which the flap nonharmonic input reduces the BVI load in the first quadrant of the sample ECR. As shown in the figure, the flap tip vorticity is reduced compared with that of the reference state due to the nonharmonic input reducing the downward deflection of the sample ECR flap in the corresponding azimuth range in the second quadrant. Scheme B has a greater range of azimuthal reductions in tip vorticity than Scheme A, but since the flaps also need to be used for rotor trimming, the reductions are not as obvious as those in Scheme A. As the tip vortex moves downstream with the fluid, the intensity of the BVI in the first quadrant of the sample ECR, and in particular the intensity of blade-vortex parallel interaction, is significantly reduced due to the reduced tip vorticity in the second quadrant.

Further, Figure 15 presents a wake vorticity contour of the sample ECR over the longitudinal planes on the
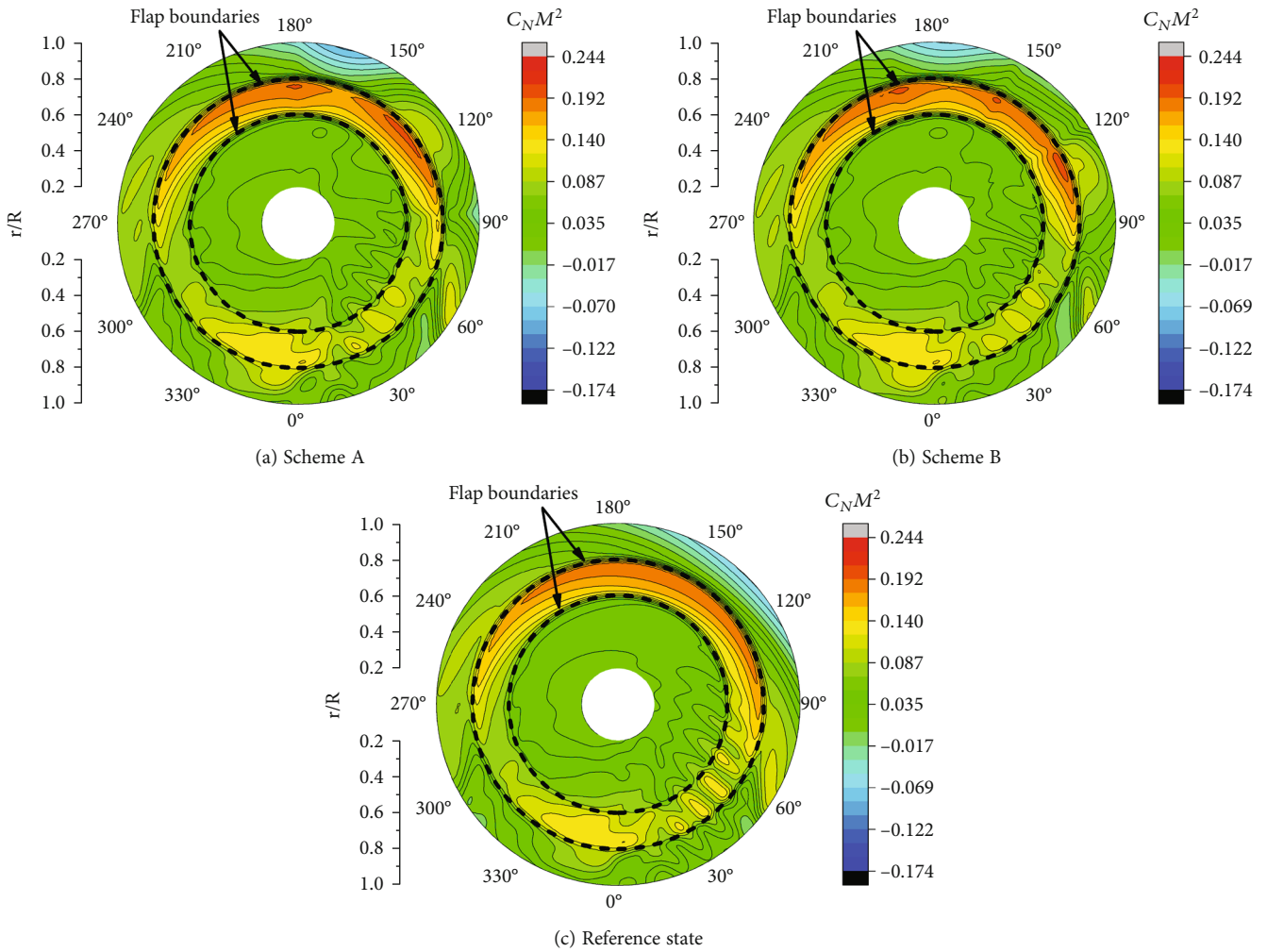
(a) Scheme A

(b) Scheme B

(c) Reference state

FIGURE 13: Effect of flap nonharmonic input on the load of ECR disc (input amplitude = −5°).
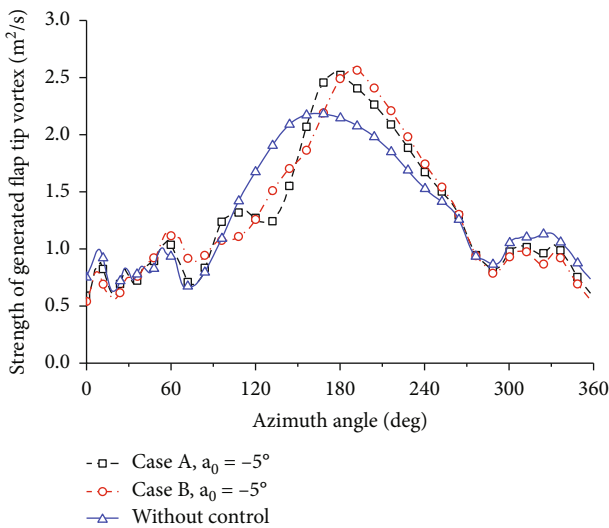

FIGURE 14: Graph of the variation in the flap tip vorticity of the sample ECR with the azimuth.

advancing side, with the location of longitudinal profile shown in Figure 15(d). According to the figure, the wake vorticity in the first quadrant $(0 < x < 1\,\mathrm{m})$ of the sample ECR is significantly reduced due to the flap nonharmonic input reducing the flap tip vorticity in the second quadrant, but the location of vortex core is not significantly different from when no nonharmonic control is applied. With consideration of the flap tip vorticity and the load distribution on the ECR disc, it is observed that the nonharmonic input reduces the intensity of flap tip vortex in the second quadrant of the ECR, resulting in a significant reduction in the BVI load intensity in the first quadrant, thus suppressing the BVI noise on the advancing side of the ECR, but it has little effect on the miss distance on the advancing side.

3.3. Nonharmonic Control of the Retreating Side BVI Load and Noise of the Sample ECR. The maximum values of SPL in the rectangular region (8m × 5.4m) below the rotor blade at 6-40 times the blade passage frequency are presented in Figure 16 for input amplitudes (a_0) 1°, 3°, 5°, and 7° of Schemes C and D. As can be seen in the figure, the maximum value of the SPL under the rotor tends to progressively

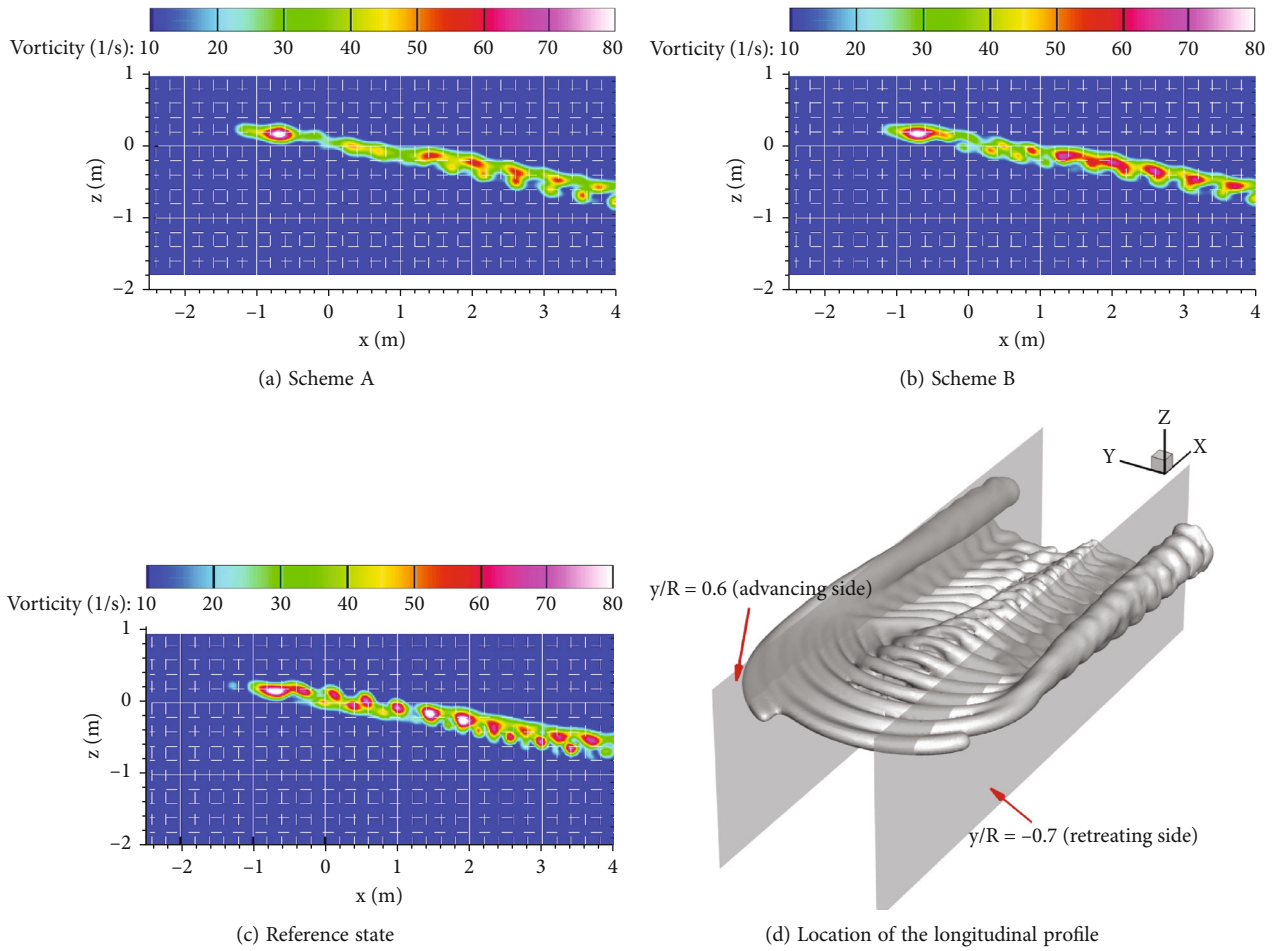(a) Scheme A

(b) Scheme B

(c) Reference state

(d) Location of the longitudinal profile

FIGURE 15: Wake vorticity cloud plot of the $y = 0.6R$ longitudinal profile on the advancing side of the sample ECR.
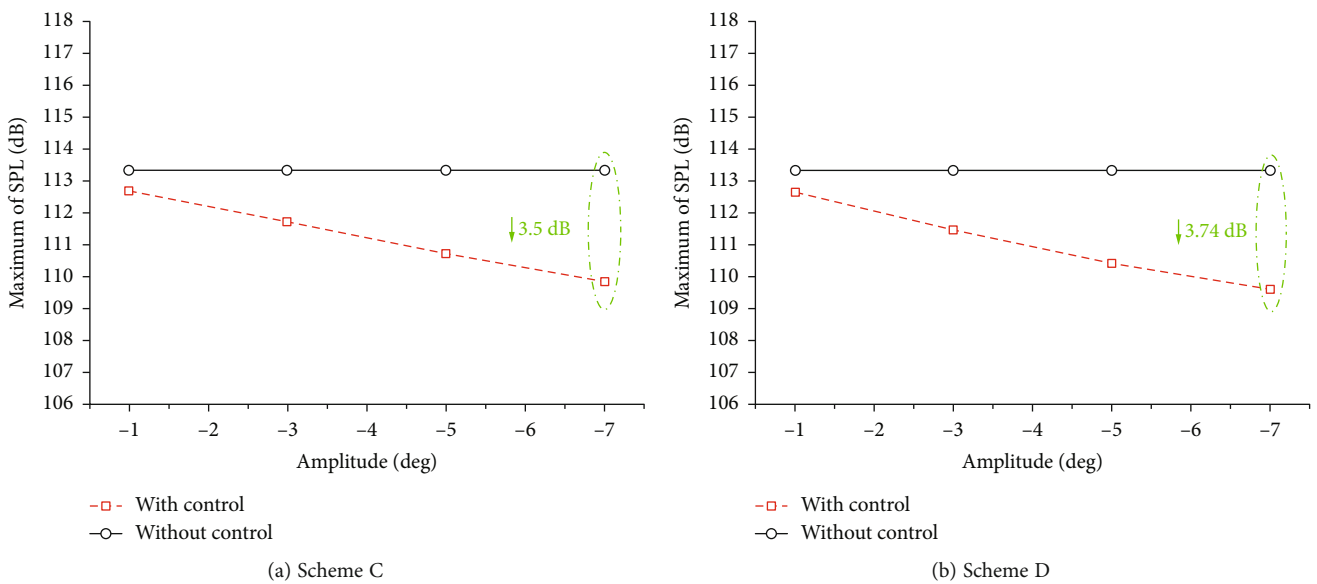

(a) Scheme C

(b) Scheme D

FIGURE 16: Effect of flap third local nonharmonic inputs in the third quadrant on maximum SPL of the noise from ECR.

(a) Distribution of sound pressure levels when $a_0 = 7°$
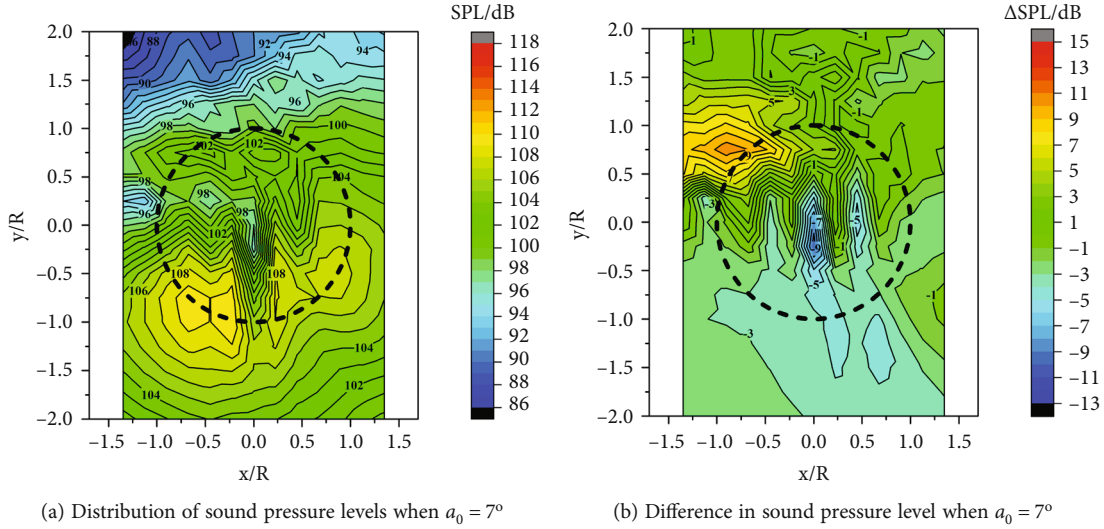
(b) Difference in sound pressure level when $a_0 = 7°$

FIGURE 17: Distribution of SPL below the ECR under Scheme C and their difference from the sound level in the reference state.

(a) Distribution of sound pressure levels when $a_0 = 7°$

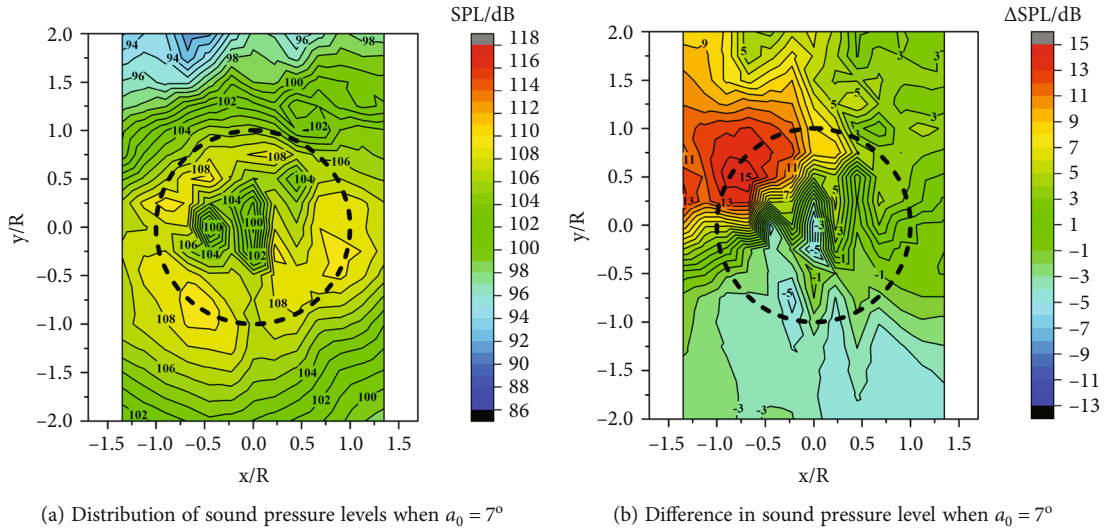(b) Difference in sound pressure level when $a_0 = 7°$

FIGURE 18: Distribution of SPL below the ECR under Scheme D and their difference from the sound level in the reference state.

decrease with increasing input amplitude for both local non-harmonic input schemes. The best control of noise beneath the sample ECR is yielded when the amplitude is 7°; the maximum SPL is reduced by approximately 3.5 dB with Scheme C and by approximately 3.74 dB with Scheme D.

Figures 17 and 18 further show the distribution of sound pressure levels in the rectangular region (8m × 5.4m) below the ECR blade at 6-40 times the blade passage frequency for various nonharmonic control schemes with an input amplitude a_0 of 7°, as well as the difference in sound pressure levels from the reference state. As can be seen from the figure, the BVI noise behind the ECR ($y/R < 0$) is reduced; however, the maximum noise reduction is found near the rotation center of the ECR, regardless of whether Scheme C or Scheme D is used for the nonharmonic input to the flap, while the noise in the region directly in front of the retreating side of electrically controlled rotor ($x/R < 0, y/R > 0$) increases to varying degrees.

For the third quadrant cosine control used in Scheme C, the peak SPL of the BVI noise on the retreating side of the ECR decreases to 109 dB when the input amplitude is 7°, while the peak BVI noise on the advancing side of the ECR does not change much, being approximately 107 dB. While the full-range cosine input in the third quadrant significantly reduces the BVI noise on the retreating side of the ECR, all noise in front of the retreating side of the rotor ($x/R < 0, y/R > 0$) increases by approximately 10 dB in front of the retreating side of the rotor. In addition, there is a significant reduction in noise of approximately 9 dB in the region directly below the rotation center of the ECR.

For the third quadrant oblique square wave input used in Scheme D, when the input amplitude is 7°, the variation pattern of the peak sound pressure level of BVI noise on the retreating side and in the region directly below the rotation center is mostly the same as that of Scheme C, but the peak

(a) Scheme C

(b) Scheme D

(c) Reference state

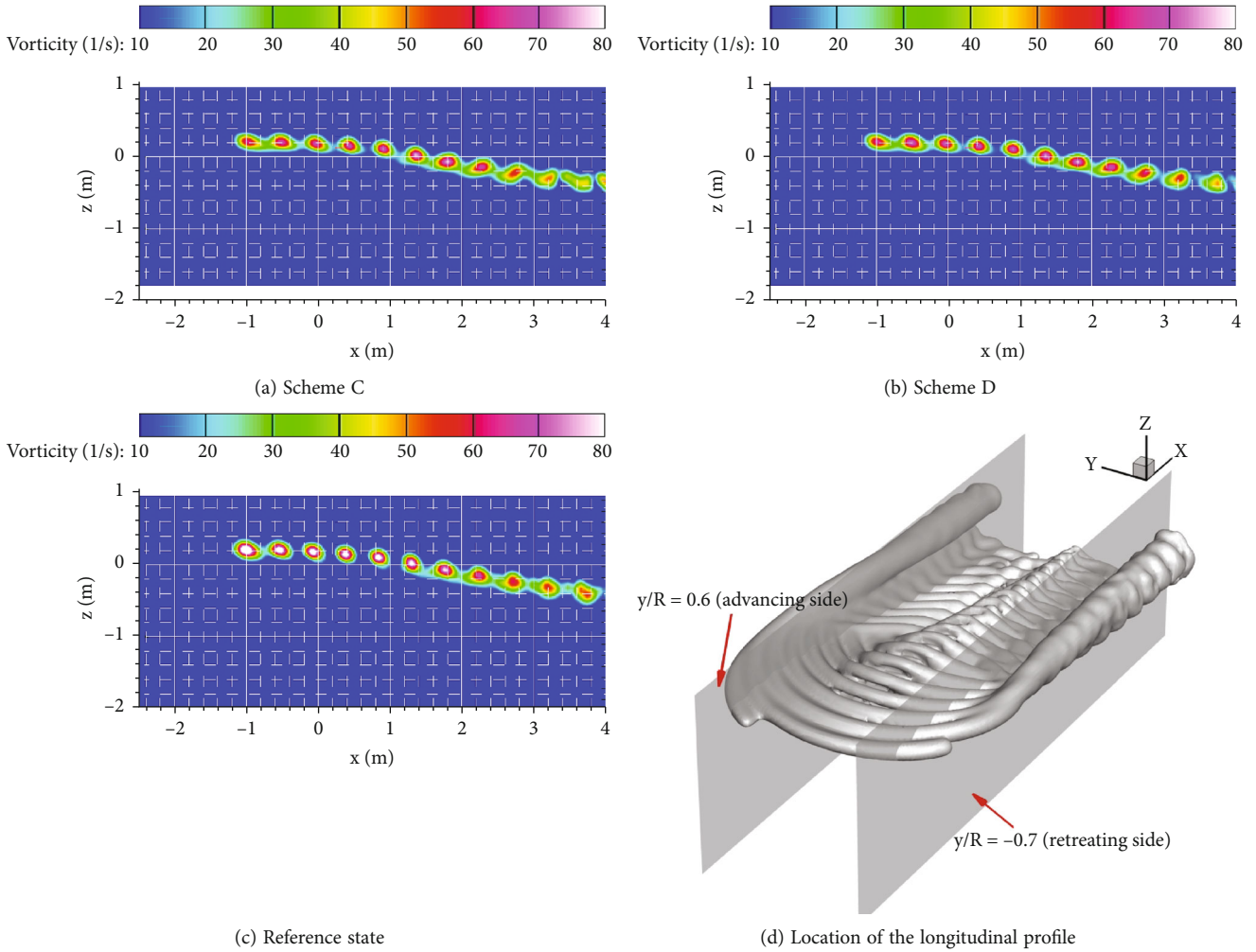(d) Location of the longitudinal profile

Figure 19: Wake vorticity cloud plot of the $y = -0.7R$ longitudinal profile on the advancing side of the sample ECR.

BVI noise on the advancing side increases to 109 dB. In addition, the nonharmonic input with Scheme D leads to an increase in noise in front of the rotor's retreating side ($x/R < 0, y/R > 0$), which increases by approximately 15 dB when the amplitude is 7°.

Further, Figure 19 presents a wake vorticity contour of the sample ECR over the longitudinal planes on the retreating side. As shown in the figure, the third quadrant nonharmonic input reduces the wake vorticity on the retreating side of the sample ECR while having almost no effect on the miss distance. This is consistent with the noise reduction mechanism of the nonharmonic input on the advancing side of the ECR, so the effect of the third quadrant flap nonharmonic input on the sample ECR disc load and the blade tip vorticity is not discussed in this paper.

3.4. Summary of the Effects of Nonharmonic Control of ECR Flaps. The noise reduction effects of the nonharmonic control of the electrically controlled rotor flaps are compared for different preinstallation angles, and the results are shown in Table 2. It is evident from the table that the use of nonharmonic control of the flaps reduces BVI-induced noise of electrically controlled rotor for var-

Table 2: Comparison of the effect of flap nonharmonic input on noise control.

Rotor type	Control scheme	Noise peak
	Reference	116.62 dB
ECR - preinstallation angle of 8°	Scheme A	112.77 dB
	Scheme B	113.86 dB
	Reference	113.35 dB
ECR - preinstallation angle of 4°	Scheme C	109.85 dB
	Scheme D	109.6 dB
ECR - preinstallation angle of 6°	Reference	115.52 dB
Conventional rotor	Reference	111.82 dB

ious preinstallation angles. When the preinstallation angle is 4°, the flap nonharmonic control under Scheme D has the best effect on the reduction in BVI-induced noise of electrically controlled rotor, which demonstrates that the BVI-induced noise of electrically controlled rotor can be reduced to a greater extent by choosing a suitable blade preinstallation angle together with the flap nonharmonic control.

4. Conclusion

In this paper, a computational model of BVI load and noise of electrically controlled rotors is developed using the viscous vortex particle method, the Weissinger-L blade model, and the FW-H equation, on the basis of which the effects of various flap nonharmonic control schemes on the control of BVI load and noise on the advancing side and retreating side of the ECR are investigated. Based on the differences in BVI characteristics of ECR at different preindex angles, the effects of the second quadrant cosine control and the second quadrant oblique square wave control on the BVI noise on the advancing side of the sample ECR are first analyzed during a sample ECR with a preindex angle of 8°; then, the mechanism of flap nonharmonic control to reduce BVI noise on the advancing side of an ECR is analyzed based on the load distribution on the sample ECR disc, the blade tip vorticity, and the longitudinal profile wake vorticity on the advancing side; on this basis, the effects and the noise reduction mechanism of the third quadrant cosine control and oblique square wave control on the retreating side of sample ECR are investigated with an ECR with a preindex angle of 4° as the object of study. Our conclusions are detailed as follows:

(1) In the control of BVI noise on the advancing side of the sample ECR, both forms of flap nonharmonic control are used to reduce the overall noise level below the rotor, but both inevitably enhance the noise ahead of the advancing side of the ECR; this is principally due to the nonharmonic input to the flap at the applied start and end azimuths resulting in dramatic changes in the load distribution on rotor disc. In both schemes, the second quadrant cosine control provides better noise reduction than the oblique square wave input; when the input amplitude is -5°, the second quadrant cosine input reduces the maximum noise below the rotor by 3.85 dB, and the peak BVI-induced noise behind the advancing side of the rotor by approximately 11 dB. Analysis of the noise reduction mechanism of the flap nonharmonic input reveals that the nonharmonic input suppresses the advancing side BVI noise principally by reducing the wake vortex strength on the advancing side of the sample ECR but has little effect on the miss distance of BVI

(2) In the control of BVI noise on the retreating side of the ECR, both forms of flap nonharmonic input are used to reduce the overall noise level below the rotor, but both inevitably enhance the noise ahead of the retreating side of the ECR. The third quadrant cosine input can reduce the maximum noise under the rotor by 3.5 dB when the input amplitude is 7° and the peak BVI-induced noise on the retreating side of the rotor to 109 dB; the third quadrant oblique square wave input results in an overall noise reduction of 3.74 dB below the rotor and reduces the peak BVI noise to 109 dB on the retreating side of the rotor. In terms of the overall level of noise under

the rotor, the two schemes are comparable. Analysis of the longitudinal profile wake vorticity on the retreating side suggests that the flap nonharmonic input reduces the BVI-induced noise on the retreating side of the sample ECR in the same way as it does on the advancing side

(3) The BVI noise of an ECR can be reduced to a greater extent by choosing a suitable blade preindex angle together with flap nonharmonic control

Data Availability

The data that support the findings of this study are available from the corresponding author (Taoyong Su) upon reasonable request.

Conflicts of Interest

The authors declare that there is no conflict of interest regarding the publication of this paper.

Acknowledgments

References

[1] T. Y. Su and Y. Lu, "Application of viscous vortex particle method to electrically controlled rotor wake and aerodynamic characteristics analysis," in *Proceeding of the 7th Asian/Australian rotorcraft forum*, pp. 2018–006, Jeju Island, Korea, 2018.

[2] R. A. Ormiston, "Aeroelastic considerations for rotorcraft primary control with on-blade elevons," in *Proceedings of the 57th American Helicopter Society Annual Forum*, pp. 57–00011, Washington, DC, USA, 2001.

[3] J. W. Shen and I. Chopra, "Swashplateless helicopter rotor with trailing edge flaps," *Journal of Aircraft*, vol. 41, no. 2, pp. 208–214, 2004.

[4] T. Y. Su, Y. Lu, J. C. Ma, and S. J. Guan, "Aerodynamic characteristics analysis of electrically controlled rotor based on viscous vortex particle method," *Aerospace Science and Technology*, vol. 97, article 105645, 2020.

[5] J. W. Shen and I. Chopra, "A parametric design study for a swashplateless helicopter rotor with trailing edge flaps," *Journal of the American Helicopter Society*, vol. 49, no. 1, pp. 43–53, 2004.

[6] Y. Lu and C. Wang, "Active control for performance enhancement of electrically controlled rotor," *Chinese Journal of Aeronautics*, vol. 28, no. 5, pp. 1494–1502, 2015.

[7] K. S. Brentner and F. Farassat, "Modeling aerodynamically generated sound of helicopter rotors," *Progress in Aerospace Sciences*, vol. 2003, no. 39, pp. 83–120, 2003.

[8] W. Johnson, *Rotorcraft Aeromechanics*, Cambridge University Press, New York, NY, USA, 2013.

[9] F. H. Schmitz, G. Gopalan, and B. W. Sim, "Flight-path management/control methodology to reduce helicopter blade-

vortex interaction noise," *Journal of Aircraft*, vol. 39, no. 2, pp. 193–205, 2002.

[10] B. Munsky and F. Gandhi, "Analysis of helicopter blade-vortex interaction noise with flight path or attitude modification," *Journal of the American Helicopter Society*, vol. 50, no. 2, pp. 123–137, 2005.

[11] R. D. Janakiram, "NASA/AHS rotorcraft noise reduction program: McDonnell Douglas helicopter company accomplishments," *Vertiflite*, vol. 43, pp. 64–68, 1988.

[12] W. R. Mantay, P. A. Shidler, and R. L. Campbell, "Some results of testing of a full-scale ogee-tip rotor," *Journal of Aircraft*, vol. 6, no. 3, pp. 215–221, 1979.

[13] V. L. Wells and A. T. Glinka, "The flip tip – a novel method for reducing blade-vortex interaction noise," in *Innovation in Rotorcraft Technology, Proceedings of the Royal Aeronautical Society*, pp. 11.1–11.11, London, UK, 1997.

[14] F. J. Perry, A. F. Jones, and P. G. Wilby, "The BERP rotor – how does it work, and what has it been doing lately," *Vertiflite*, vol. 44, no. 2, pp. 44–48, 1998.

[15] J. Feinerman, S. Koushik, and F. H. Schmitz, "Effect of leading-edge serrations on helicopter blade-vortex interaction noise," in *67th Annual Forum of the American Helicopter Society*, pp. 2001–003, Virginia Beach, VA, USA, 2011.

[16] S. Dawson, M. Marcolin, E. Booth et al., "Wind tunnel test of an active flap rotor: BVI noise and vibration reduction," in *51st Annual Forum of the American Helicopter Society*, pp. 1995–045, Fort Worth, TX, USA, 1995.

[17] M. Hofinger and P. Leconte, "Development of an active flap rotor model," in *6th ONERA-DLR Aerospace Symposium*, pp. 129–140, Berlin, Germany, 2004.

[18] P. Crozier, P. Leconte, Y. Delrieux, B. Gimonet, A. L. Pape, and H. M. Rochttes, "Wind tunnel tests of a helicopter rotor with active flaps," in *32nd European Rotorcraft Forum*, pp. 1–16, Maastricht, The Netherlands, 2006.

[19] Y. Delrieux, A. L. Pape, P. Crozier, B. Gimonet, and H. M. Rochettes, "Wind tunnel assessment of the concept of active flaps on a helicopter rotor model," in *63rd Annual Forum of the American Helicopter Society*, pp. 2007–000052, Virginia Beach, VA, USA, 2007.

[20] R. D. Janakiram, B. W. Sim, and C. K. Kitaplioglu, "Blade-vortex interaction noise characteristics of a full-scale active flap rotor," in *65th Annual Forum of the American Helicopter Society*, pp. 2009.1–2009.21, Grapevine TX, USA, 2009.

[21] F. K. Straub, V. R. Anand, B. H. Lau, and T. S. Birchette, "Wind tunnel test of the SMART active flap rotor," *Journal of the American Helicopter Society*, vol. 63, no. 1, pp. 1–16, 2018.

[22] D. Patt, L. Liu, and P. P. Friedmann, "Helicopter noise reduction by actively controlled flaps," in *11th AIAA/CEAS Aeroacoustics Conference*, pp. 2005–2904, Monterey, California, 2005.

[23] D. Patt, L. Liu, and P. P. Friedmann, "Simultaneous vibration and noise reduction in rotorcraft using aeroelastic simulation," *Journal of the American Helicopter Society*, vol. 51, no. 2, pp. 127–140, 2006.

[24] P. P. Friedmann, "On-blade control of rotor vibration, noise, and performance: just around the corner? The 33rd Alexander Nikolsky honorary lecture," *Journal of the American Helicopter Society*, vol. 59, no. 4, pp. 1–37, 2014.

[25] T. Y. Su, Y. Lu, J. C. Ma, and S. J. Guan, "Electrically controlled rotor blade vortex interaction airloads and noise analysis using viscous vortex particle method," *Shock and Vibration*, vol. 2019, Article ID 9678970, 15 pages, 2019.

[26] C. J. He and J. G. Zhao, "Modeling rotor wake dynamics with viscous vortex particle method," *AIAA Journal*, vol. 47, no. 4, pp. 902–915, 2009.

[27] J. F. Tan and H. W. Wang, "Simulating unsteady aerodynamics of helicopter rotor with panel/viscous vortex particle method," *Aerospace Science and Technology*, vol. 30, no. 1, pp. 255–268, 2013.

[28] Y. J. Shi, G. H. Xu, and P. Wei, "Rotor wake and flow analysis using a coupled Eulerian-Lagrangian method," *Engineering Applications of Computational Fluid Mechanics*, vol. 10, no. 1, pp. 384–402, 2016.

[29] P. Singh and P. P. Friedmann, "Application of vortex methods to coaxial rotor wake and load calculations in hover," *Journal of Aircraft*, vol. 55, no. 1, pp. 373–381, 2018.

[30] J. F. Tan, T. Y. Zhou, Y. M. Sun, and G. N. Barakos, "Numerical investigation of the aerodynamic interaction between a tiltrotor and a tandem rotor during shipboard operations," *Aerospace Science and Technology*, vol. 87, pp. 62–72, 2019.

[31] Y. Lu, T. Y. Su, R. L. Chen, P. Li, and Y. Wang, "A method for optimizing the aerodynamic layout of a helicopter that reduces the effects of aerodynamic interaction," *Aerospace Science and Technology*, vol. 88, pp. 73–83, 2019.

[32] I. E. Garrick, *Propulsion of a flapping and oscillating airfoil*, NACA TR, 1936.

[33] J. G. Leishman and T. S. Beddoes, "A generalized method for unsteady airfoil behavior and dynamic stall using the indicial method," in *Proceedings of the 42th American Helicopter Society Annual Forum*, pp. 1986–023, Washington D.C, USA, 1986.

[34] N. Hariharan and J. G. Leishman, "Unsteady aerodynamics of a flapped airfoil in subsonic flow by indicial concepts," in *36th AIAA/ASME/ASCE/AHS/ASC Structures, Structural Dynamics, and Materials Conference*, pp. 10–12, New Orleans, LA, USA, 1995.

[35] F. Farassat, *Theory of noise generation from moving bodies with an application to helicopter rotors*, NASA TR R-451, 1975.

[36] M. J. Smith, J. W. Lim, B. G. Wall et al., "An assessment of CFD/CSD prediction state of the art using the HART II international workshop data," in *Proceedings of the 68th American Helicopter Society Annual Forum*, pp. 1–3, Fort Worth, TX, USA, 2012.